HgCdTe avalanche photodiode array detectors with single photon sensitivity and integrated detector cooler assemblies for space lidar applications

Xiaoli Sun
James B. Abshire
Michael A. Krainak
Wei Lu
Jeff D. Beck
William W. Sullivan III
Pradip Mitra
Dick M. Rawlings
Renny A. Fields
David A. Hinkley
Bradley S. Hirasuna

SPIE.

HgCdTe avalanche photodiode array detectors with single photon sensitivity and integrated detector cooler assemblies for space lidar applications

Xiaoli Sun,[a,*] James B. Abshire,[a] Michael A. Krainak,[a] Wei Lu,[b] Jeff D. Beck,[c] William W. Sullivan III,[c] Pradip Mitra,[c] Dick M. Rawlings,[c] Renny A. Fields,[d] David A. Hinkley,[d] and Bradley S. Hirasuna[d]
aNASA Goddard Space Flight Center, Greenbelt, Maryland, United States
bATA Aerospace, LLC, Greenbelt, Maryland, United States
cLeonardo DRS Electro-Optical Infrared Systems, Dallas, Texas, United States
dThe Aerospace Corporation, El Segundo, California, United States

Abstract. A HgCdTe avalanche photodiode (APD) focal plane array assembly with linear mode photon-counting capability has been developed for space lidar applications. An integrated detector cooler assembly (IDCA) has been built using a miniature Stirling cooler. A microlens array has been included to improve the fill factor. The HgCdTe APD has a spectral response from 0.9- to 4.3-μm wavelengths, a photon detection efficiency as high as 70%, and a dark count rate of <250 kHz at 110 K. The mass of the IDCA is 0.8 kg and the total electrical power consumption is about 7 W. The HgCdTe APD arrays have been characterized at NASA Goddard Space Flight Center. A series of environmental tests have been conducted for the IDCAs, including vibration, thermal cycling, and thermal vacuum tests. A description of the device and the test results at NASA are given in this paper. © *The Authors. Published by SPIE under a Creative Commons Attribution 4.0 Unported License. Distribution or reproduction of this work in whole or in part requires full attribution of the original publication, including its DOI.* [DOI: 10.1117/1.OE.58.6.067103]

Keywords: photon counting; infrared detectors; avalanche photodiodes; cryocoolers; lidar.

Paper 190134 received Jan. 29, 2019; accepted for publication May 15, 2019; published online Jun. 17, 2019.

1 Introduction

HgCdTe avalanche photodiode (APD) focal plane arrays (FPAs) have been shown to perform linear mode photon counting (LMPC) detection with >60% photon detection efficiency (PDE) from 0.9 to 4.3 μm.[1] They are nearly ideal detectors for the next generation of space lidar for measuring surface elevations, spectral absorption, atmosphere gas concentration, and atmospheric backscatter profiles. They enable airborne and spaceborne lidar systems to operate in near-to-mid-infrared laser wavelengths and to simultaneously map the surface topography and measure the spectral absorption features on the surface of airless bodies, such as volatiles on the moon, asteroids, and the cores of comets.

Goddard Space Flight Center (GSFC) collaborated with Leonardo DRS Electro-Optical Infrared Systems to mature the fabrication of the HgCdTe APD arrays and to develop cryocooler and packaging techniques for advanced space lidar systems at infrared wavelengths. As part of this work, DRS produced a batch of 4×4 pixel HgCdTe APD arrays that demonstrated nearly quantum-limited detector performance.[2] These detectors were successfully used in NASA GSFC's airborne CO_2 lidar at 1.57 μm,[3] its airborne CH_4 lidar at 1.65 μm,[4] and in the NASA Langley Research Center airborne CO_2 lidar at 2.05 μm.[5] DRS also produced a set of 2×8 pixel prototype APD arrays with lower dark current and higher APD gains, which enabled LMPC.[1,6] Recently, DRS successfully integrated a 2×8-pixel HgCdTe APD FPA with a microlens array and a mini-Stirling cooler into an integrated detector cooler assembly (IDCA).[7,8] These new HgCdTe APD arrays and the IDCAs were characterized

at both DRS and NASA GSFC and underwent environmental tests. These results support and augment the test data reported by DRS.[1,6] A brief description of the devices and the new test results are presented in this paper.

The 2×8-pixel HgCdTe APD FPAs have pixels 64×64 μm in size on a 64-μm pitch. They have shown a >60% PDE at 1.55-μm wavelength and <250-KHz noise count rate per pixel in LMPC mode operation.[6] A major portion of the dark counts is believed to come from the ambient thermal emissions leaking through gaps in the cold shield and photon emissions from the read out integrated circuit (ROIC) leaking through the gaps of the light barrier. The actual dark current of the HgCdTe APD was measured to be <30,000 electrons/s per pixel at APD gain up to 1900.[6] The analog outputs of the detectors had a single photon impulse response width of 6-ns full width at half maximum (FWHM).[6] For large signals, the output pulse amplitude was proportional to the number of photons in the received pulse. The ROIC also contains a set of built-in comparators, one for each pixel, which can be turned on to convert the analog signal for each detected photon into a digital pulse. The devices provids both analog and digital outputs. The analog outputs gives a linear sum of the pulse waveforms from all detected photons with wide dynamic range. The digital outputs can be used for single-photon-counting applications at low light level.

Two IDCAs with the 2×8 pixel FPAs were fabricated and characterized. Environmental tests were performed on these IDCAs, including a vibration test, a thermal cycle test, a thermal shock test, and a thermal vacuum test. Radiation damage tests were also performed on the FPA's from the lot, which showed that these devices can be used in the space radiation environment of a typical Earth orbiting mission, provided that the FPAs can be annealed periodically by

heating them to 85°C for a few hours.[9] The annealing can be achieved by including a small heater on the chip carrier inside the Dewar.

2 HgCdTe Avalanche Photodiode Linear Mode Photon Counting Focal Plane Array

2.1 HgCdTe Avalanche Photodiode Arrays

The DRS LMPC HgCdTe APD arrays use the high-density vertically integrated photodiode (HDVIP®) architecture, which is shown in Fig. 1.[10–13] Each element is a p-around-n cylindrical photodiode formed around a small via in the HgCdTe film on the silicon substrate. Each pixel consists of four photodiodes connected in parallel. The same pixel structure can be replicated into an array of pixels of desired format. HgCdTe APDs have a wide spectral response from the visible to the cutoff wavelength determined by the mole fraction x of CdTe in $Hg_{1-x}Cd_xTe$.

Photoelectrons are generated from the photons incident on the HgCdTe material. They diffuse laterally to the p–n junction and are multiplied by the APD gain. The diffusion time for each photoelectron is random and depends on where the photon is absorbed. As a result, there is a random time delay, or timing jitter, in the output pulses. Most of the photoelectrons are generated in the p-region and experience full gain since they traverse the entire length of the gain region. Photoelectrons generated inside the APD gain region, the n-region around the via, do not experience the full APD gain and may not be counted. Photons that fall inside the

via are not detected. The optimal region for photon counting is the circular area between the four diodes, as shown in Fig. 1. For the 64-μm pixel devices at high APD gain, the center optimal diameter is about 22 μm. Areas outside the optimal area around and between the n-regions are also sensitive to single photons, though irregular in shape.

The LMPC HgCdTe APD arrays, which we tested, had a quantum efficiency of >90% from visible to the cutoff wavelength of 4.3 μm.[6] The APD preamplifiers in the ROIC in these devices were mounted directly underneath the HgCdTe APD array to minimize the input stray capacitance. A light barrier was also included between the ROIC and the HgCdTe APD array to minimize the detection of photons emitted by the circuitry in the ROIC unit cell.[6] The APD gain was set sufficiently high that the amplitude of the photocurrent pulse from each absorbed photon was many times the noise floor of the electronics. The APD gain for each primary photoelectron was nearly constant and the excess noise factor was near unity.[11–13] The output pulse waveform was the sum of individual photoelectron pulses and the linearity was limited by the readout electronics.[2]

The prototype devices were designed to have a 2×8-pixel format. There was a guard ring around the array that consisted of a single row or column of pixels biased at the same voltage but not connected to the output terminals. The purpose of the guard ring was to surround each pixel with the same boundary conditions to achieve a uniform response. Larger arrays with more pixels can be fabricated, provided there are sufficient input and output pins on the chip carrier and sufficient number of feed-through connections in the cryocooler housing.
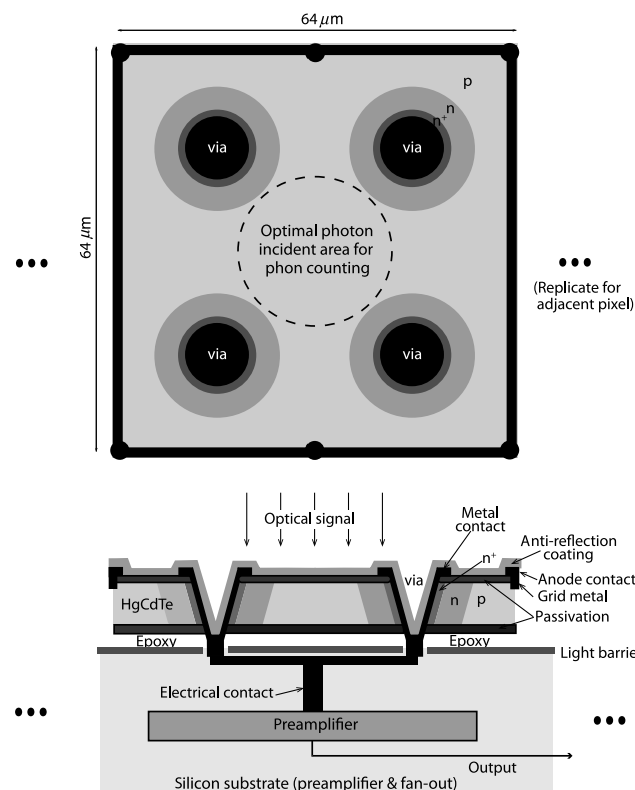
2.2 Readout Integrated Circuit

The preamplifiers in the ROIC were located directly under the HgCdTe APDs, as shown in Fig. 1. There were 16 channels, one for each pixel, and each consisted of a transimpedance amplifier and a unity gain buffer amplifier. The transimpedance gain could be adjusted from 100 to 500 kV/A but nominally it was set to about 200 kV/A for photon-counting operation. The electrical bandwidth of the ROIC was about 40 MHz,[1] which was mainly limited by the parasitic capacitance.[6] The equivalent input noise current spectral density of the transimpedance preamplifier was about 1.5 pA/Hz$^{1/2}$, which became negligible when the APD gain is >500. More detailed description of the LMPC HgCdTe APD array and the ROIC can be found in Refs. 1 and 6.

2.3 Cryocoolers

For proper operation, the HgCdTe APD FPAs needed to be held between 77 and 130 K. Liquid nitrogen Dewars were used in the laboratory to characterize the devices. For airborne and spaceborne applications the mini-Stirling cryocoolers by DRS were selected which were originally developed for military applications and demonstrated to survive a rocket launch. These mini-Stirling coolers had also demonstrated multiyear lifetimes.[14,15] We previously studied the use of a pulse-tube cryocoolers, such as the microcooler from Northrop Grumman.[16] A pulse-tube cooler has a higher efficiency, lower vibration, longer lifetime, but high cost. Both types of cryocoolers are suitable for this application.
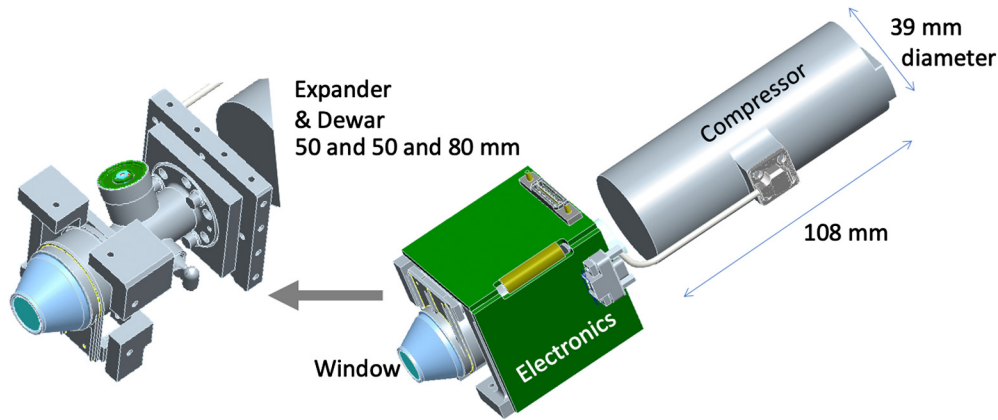

Fig. 1 Schematic representation of a LMPC pixel of HgCdTe APDs by DRS using the HDVIP® p-around-n cylindrical device structure. The APD gain regions are the n-regions around the via. The detectors are vertically integrated to preamplifiers in the underlying silicon ROIC to reduce the stray capacitance.

Fig. 2 The DRS mini-Stirling cryocooler for the 2×8-pixel FPA.

An IDCA was developed under the NASA In-space Validation of Earth Science Technology (InVEST) program.[7] It consisted of a 2×8-pixel LMPC HgCdTe array and a 0.2-W mini-Stirling cooler from DRS,[14] as shown in Fig. 2. The net weight of the IDCA was about 0.8 kg, including the peripheral electronics. In vacuum, its total electrical power consumption was between 4 and 7 W, depending on the heat sink temperature. The signal buffer amplifiers and the control electronics were mounted on the expander.

2.4 Microlens Arrays

The microlens arrays were included in the IDCA developed for the NASA InVEST program. These were used to concentrate the incident light onto the center regions of the pixels and improve the fill factor to nearly 100%. The trade-off was that the microlens arrays restrict the incident angle of the input optical signals onto the detector,[17] which limited the lidar receiver aperture size and field of view. The microlens arrays were designed and fabricated by Jenoptik with a 2×8 pattern that matched that of the detector pixels. To achieve maximum fill factor, the microlens array was placed at the focal distance from the detector and the incident light was focused on the top of the microlenses.[17] Since this was the first time we installed a microlens array on the HgCdTe APD arrays, we selected a relatively long focal length, i.e., 60 μm. It provided a sufficient spacing and tolerance between the microlens array and the HgCdTe APD array during the installation and vibration tests. The acceptance angle of the detector with this microlens array was $f/7$, which was suitable for our application. In future applications, the focal length of the microlens array could be reduced to increase the light acceptance angle.

3 Test Results of the HgCdTe Avalanche Photodiode Detector in Liquid Nitrogen Dewar

The LMPC HgCdTe APD FPAs were evaluated extensively at DRS,[1,6] prior to their delivery to NASA GSFC. Here, we report the results obtained at NASA GSFC using a different test setup. We first describe the test results obtained for the HgCdTe APD FPA in a liquid nitrogen Dewar, which allowed more flexibility in test configuration, such as changing the cold shield size and numerical aperture. We then describe the environmental test results obtained for the HgCdTe APD array in a packaged IDCA. All the test results were obtained from the analog outputs of the devices since we could directly measure the detector output pulse characteristics and more conveniently convert them into digital outputs with external comparators.

3.1 Test Setup

The test setup used for detector characterization at GSFC is shown in Fig. 3. There were two test lasers used, a generic continuous wave (cw) laser and a pulsed laser with width <0.1 ns, both emitting at 1.55-μm wavelength. The light spot on the detector was about 5 μm in diameter at $1/e^2$ points. The focusing optics assembly was mounted on an X–Y translation stage that was controlled by a computer to scan the light spot across the detector in 1-μm steps. An optical fiber attenuator was used to adjust the signal power. There was also a fixed attenuator (30 dB) in the collimated space of the focusing optics assembly. Both attenuators were calibrated before the measurements. The optical signal power onto the detector at 0-dB attenuation was calibrated by replacing the detector with the optical
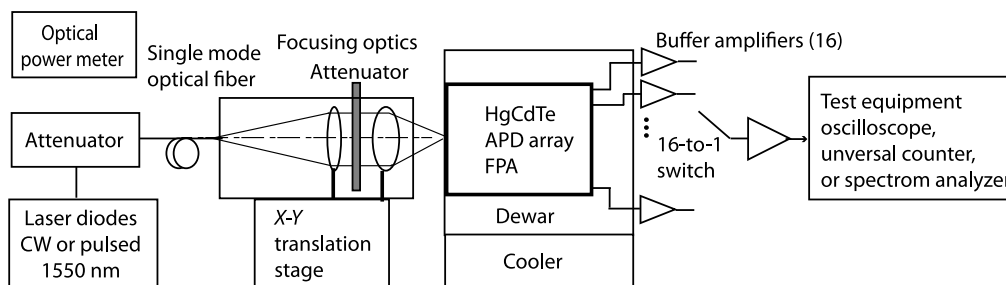

Fig. 3 Block diagram of the test setup for detector characterization at GSFC. The cooler is either a liquid nitrogen Dewar during the initial characterization or a mini-Stirling cryocooler for the IDCA testing.

power meter head with the optical fiber attenuator set to 0 dB and the fixed attenuator removed. A 16-to-1 switch was used to select the pixel output to measure. In addition, a linear amplifier with a voltage gain of 5 was added to further amplify the signal above the noise floor of the test equipment.

3.2 Responsivity and Avalanche Photodiode Gain

The detector responsivity of a single pixel was measured as a function of the APD bias voltage using the cw laser. A mechanical chopper was used between the focusing lenses and the Dewar window. The signal being measured was the difference of the buffer amplifier output with light blocked and unblocked by the chopper. The use of the chopper helped to determine and subtract the baseline from a relatively weak signal. The actual APD bias was the sum of the external bias voltage and the 0.9 V DC offset at the input of the preamplifiers. In the remainder of this paper we refer to the APD bias voltage as the voltage applied externally, not including the 0.9 V from the preamplifier DC offset. Since the photoelectron multiplication gain of the HgCdTe APDs is unity at a net bias of <1.0 V bias voltage,[2,11] the APD gain at other bias voltages can be obtained by dividing the responsivity at a given bias voltage by that at zero external bias voltage. Figure 4 plots both the responsivity of a typical pixel, excluding the gain of the external linear amplifier, and the APD gain as a function of the bias voltage. The output became saturated at APD bias voltage above 9 V. The APD was designed to detect short laser pulses and the bias circuit might have been drained under this relatively high and near cw illumination (10 pW/pixel). The APD gain should continue to increase exponentially with the bias voltage to beyond 1000 if it was not saturated,[6] as shown by the dotted line and crosses in Fig. 4. The HgCdTe APD quantum efficiency was estimated to be about 90% from these measurements, assuming unity APD gain at 0 V bias, preamplifier gain of 200 kV/W, external linear amplifier gain of 5, and 1-dB cable loss.
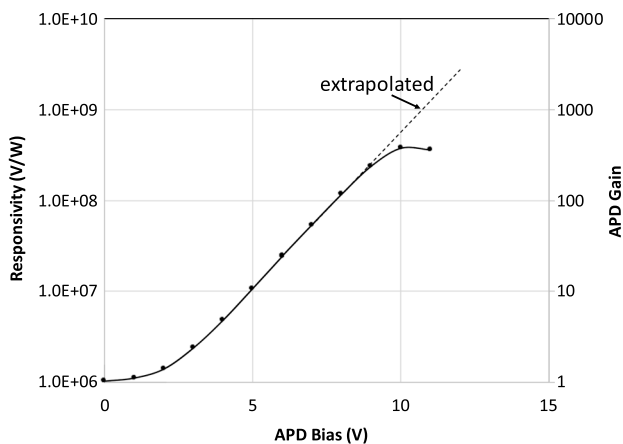
3.3 Noise Equivalent Power

The detector's output noise spectra were measured using a radio frequency (RF) spectrum analyzer. Figure 5 shows the noise output from a single pixel under the conditions of a relatively strong cw laser light illumination at 11.5-V APD bias voltage. The net noise spectral density in response to the illumination is also plotted. The detector's electrical bandwidth can be estimated as the frequency where the net illuminated noise power density drops by 3 dB, which is about 40 MHz in this case. According to a Silvaco Hipex software analysis,[6] the bandwidth is mainly limited by the parasitic effects and may be improved in future development.

The detector noise density was measured as a function of the APD bias voltage. The detector noise equivalent power (NEP) was calculated by converting noise power to the root mean square (rms) voltage noise in $V/Hz^{1/2}$ at 20 MHz and then dividing it by the responsivity, as shown in Fig. 6.
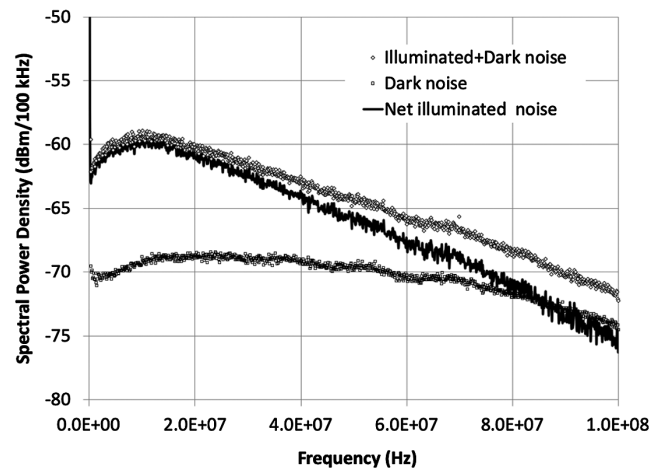

Fig. 5 Detector output noise spectral density at 11.5-V APD bias under a relatively strong illumination and dark conditions, and the difference of the two from Pixel (R2:C3) of FPA-A8327-8-2. The noise spectral densities shown are the actual measurements by the spectrum analyzer, including the gain of the linear amplifier before the test equipment.
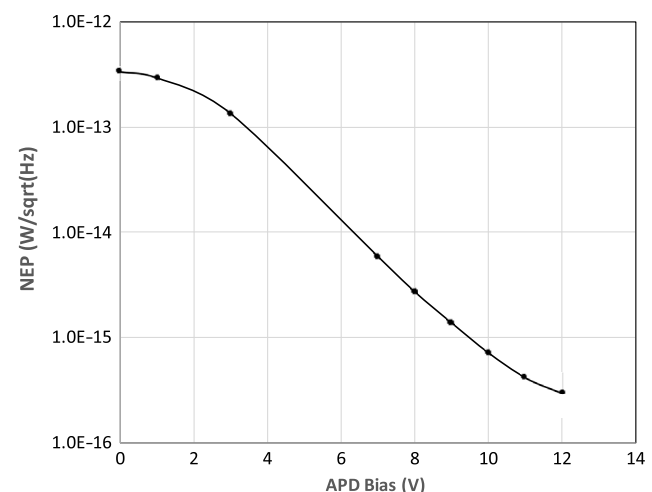

Fig. 4 Measurement of the detector responsivity and the APD gain as a function of the APD bias voltage from one of the pixels, (R2:C3) of FPA-A8327-8-2, using a 1.55-μm cw laser and a mechanical chopper. The dotted line in the plot shows the extrapolated APD gain for low-duty cycle laser pulse illumination.

Fig. 6 The NEP versus APD bias voltage from Pixel (R2:C3) of FPA-A8327-8-2.

When the APD bias was >11 V, the NEP became sufficiently low to allow single photon detection. The NEP was 0.3 fW/Hz$^{1/2}$ at the maximum applied reverse bias of 12 V.

3.4 Pulse Response and Timing Jitter

The detector's analog output pulse waveforms were measured by using the short pulse laser at 1.55 μm and a high-speed oscilloscope. Figure 7 shows the measured pulse waveforms under 1, 4, and 16 average incident photons/pulse at 11.5 V APD bias. The oscilloscope was triggered by the synchronization pulses from the laser that were coincident with the laser pulse emissions. Because the laser pulse width was narrow (<0.1 ns) compared to the detector output pulse width, the photons could be assumed to arrive at the same time.

As expected, the detector output pulse waveforms appeared at about the same time on the oscilloscope with a fixed delay but randomly varying amplitudes. The fluctuation of the pulse amplitude was due to the statistical nature of the photon detection and the randomness of the APD gain. The signal pulse amplitude increased with the incident laser pulse energy, while the amplitude of the dark noise and background photons remained at single photoelectron level and became negligible as the incident signal pulse energy increased. The pulse rise time and fall time were measured to be 3.2 and 7.4 ns, respectively. The pulse width was about 6 ns FWHM.

The timing jitter of the detector output was measured at 50% pulse rise time, which was the time from the oscilloscope triggering pulse to the threshold crossing time of the pulse waveform at 50% pulse amplitude. It was measured using the "time-to-level" function of a digital oscilloscope (LeCroy Wavepro 7Zi). The oscilloscope was programmed to measure the arrival times of only those pulses which were likely to come from the incident laser pulses, i.e., within a window of 3- to 4-ns pulse rise time and slightly above the average noise floor. The results from one of the devices (FPA-A8327-14-1) are shown in Fig. 7. The measured jitters were 0.42, 0.36, and 0.27 ns under the incident signal level of 1, 4, and 16 average photons per pulse, respectively.
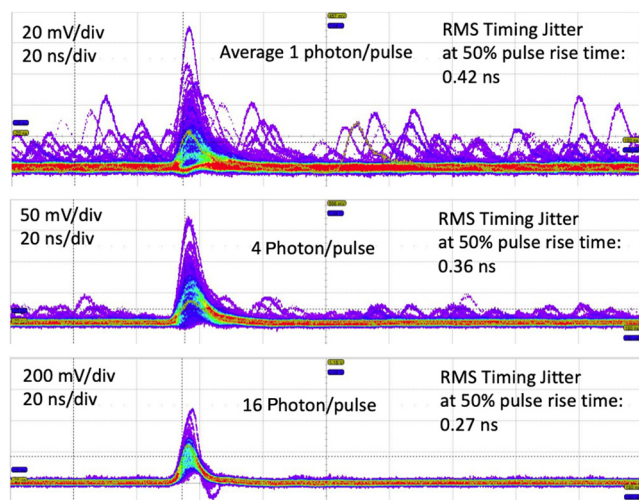
We also measured the timing jitter of a device with a slightly different doping (FPA-A8327-8-2) and nearly twice the APD gain. The timing jitter was 20% to 60% higher. The measured timing jitter data were also affected by the occasional noise pulses within the window and the electronic noise at the threshold crossing. This was part of the reason why the measured timing jitters decreased as the incident signal level increased.

These timing jitter measurements were made with the detectors being flood-illuminated by the laser. As a result, photons arrived randomly within the detector active area and the measurement results consisted of the arrival times of photoelectrons from different locations within the active area and hence with different diffusion times. The measured timing jitter distribution is expected to be more uniform if the incident light is focused on the center spot of the detector active area. We also measured the timing jitter with the laser light focused onto a 5-μm spot near the center of the pixel illuminated by several thousand photons/pulse at unity 0 V APD bias (unity gain). The effects of the APD gain fluctuation and electronics noise should be negligible in this case. The timing jitter was measured to be 80 ps.

The amount of time jitter from these measurements was significantly less than those reported by us earlier.[6] We found two causes for the discrepancy. First, the test laser which we used earlier had a 1-ns FWHM pulse width and the effect of the test laser's pulse width was not compensated for in the results. Second, the timing jitter values reported earlier were measured with the leading-edge threshold crossing detection at a fixed threshold value, which was affected by the pulse amplitude fluctuation or range walk. The results we report here were measured at a fixed fraction of the pulse amplitude, as with a constant fraction discriminator commonly used in photon-counting applications.

3.5 Analog Output Dynamic Range and Excess Noise Factor

We characterized the dynamic range of the detector analog output by measuring the pulse amplitude as a function of the incident laser photons/pulse at 0, 7.5, and 11.5 V APD bias using the same short-pulsed laser over a range of the input optical signal levels. The mean and standard deviation of the pulse amplitude of the measurement results are plotted in Fig. 8. The dynamic range of the detector output at each APD gain setting was about two orders of magnitude at each APD bias setting. With the adjustment of the APD bias voltage, the total detector output dynamic range can be extended to about five orders of magnitude.

The APD gain excess noise factor, F_{ex}, can be found from the above data according to the following equation:[2]

$$\text{SNR} \equiv \frac{\mu_{\text{sig}}}{\sigma_{\text{sig}}} = \frac{\eta_{QE} \langle G \rangle \langle n_{\text{sig}} \rangle}{\sqrt{\eta_{QE} F_{ex} \langle G \rangle^2 \langle n_{\text{sig}} \rangle + \sigma_{\text{dark}}^2}}, \quad (1)$$

where μ_{sig} and σ_{sig} are the mean and standard deviation of the output pulse amplitude, η_{QE} is the detector quantum efficiency assumed to be 90%, $\langle G \rangle$ is the average APD gain, $\langle n_{\text{sig}} \rangle$ is the average number of incident photons in the laser pulses, and σ_{dark}^2 is the variance of the dark noise. The resulting excess noise factor at 11.5 V APD bias voltage is plotted in Fig. 9.
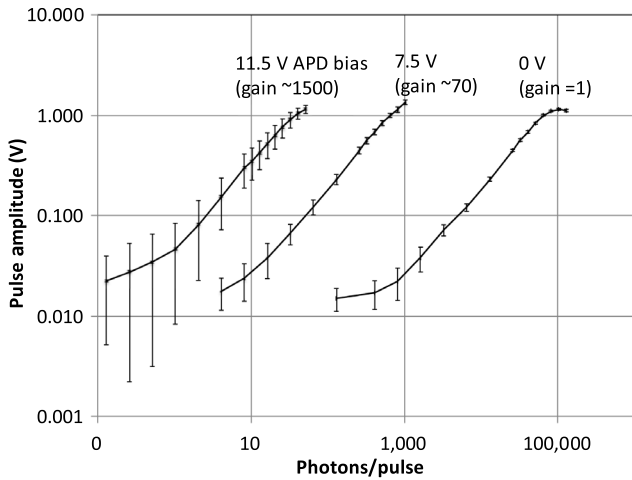

Fig. 7 Output pulse waveform from a single pixel (R2C6) of FPA-A8327-14-1 in response to a narrow pulse width (<0.1 ns) laser illumination at 11.5 V APD bias.

Fig. 8 Detector output dynamic range measurements from Pixel (R2:C3) of FPA-A8327-8-2 under a narrow pulse width (<0.1 ns) laser illumination at 0, 7.5, and 11.5 V APD bias.
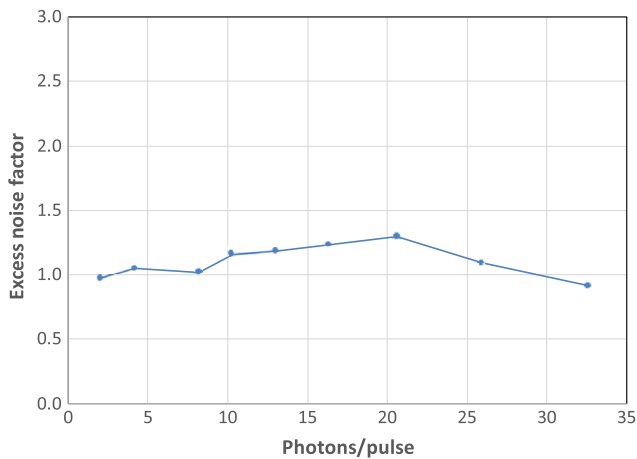

Fig. 10 Total measured, dark, and net photon count rates versus the incident photon rates from two adjacent pixels of FPA-A8327-8-2 at the optimal discriminator threshold level and an APD bias of 11.5 V.

Fig. 9 APD excess noise factor of FPA-A8327-8-2 at 11.5 V APD bias.

Fig. 11 PDE versus FER of FPA-A8327-14-1, pixel (1,6), over a range of APD bias voltage.

3.6 Photon-Counting Performance

The detectors are suitable for single photon counting with the use of a discriminator (comparator) and the APD gain set to >500. Figure 10 shows the measured count rates with the detector in dark, under illumination from the cw laser, and the difference of the two. The APD bias was set to 11.5 V and the discriminator threshold is set to the value for which the photon detection efficiency (PDE) just reached the maximum value but without further increasing the false event rate (FER). The results from the two pixels are plotted and they are nearly the same. The dark count rate was about 250 kHz. The PDE was as high as 70%, based on this test result. The detected photon count rate starts to saturate at about 10^7 counts/s, which is limited by the electrical bandwidth. Pulse waveforms from the analog outputs can be used to extend the dynamic range when needed. Note that PDE is a measure for single photon detection using a comparator. It is always lower than the quantum efficiency because not all the photons absorbed result in pulse amplitude exceeding the comparator threshold and consequently being counted.
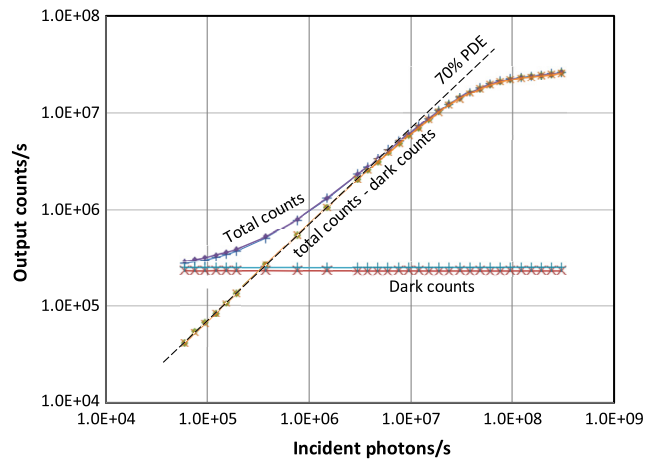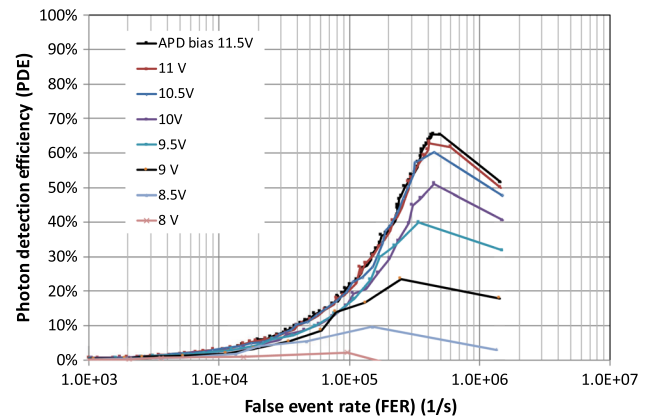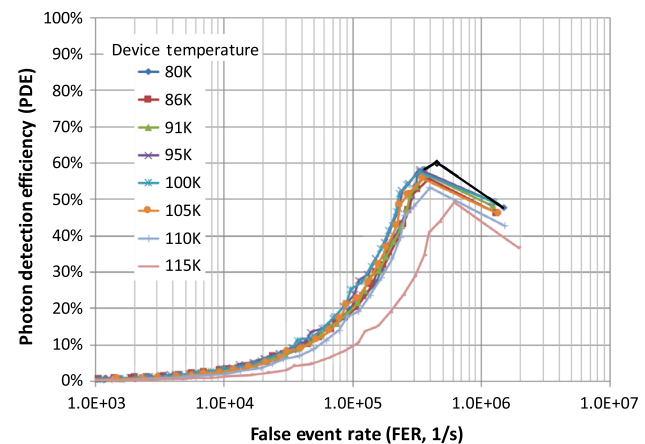

Fig. 12 PDE versus FER of FPA-A8327-14-1, pixel (1,6), over a range of device temperature. The APD bias voltage is set to 11.5 V.

The PDE versus FER was measured over a range of discriminator thresholds at different APD bias voltage from another device and the results are plotted in Fig. 11. The PDE and FER increase as the discriminator threshold

decreases. Similar results were obtained at DRS using a digital oscilloscope and waveform-processing software.[6] The results in Fig. 11 show that the APD photon-counting performance improves as the APD bias voltage, and hence the gain increases, and approaches optimal performance when the bias is above 10.5 V.

The PDE versus FER were measured again at different device temperatures at a fixed APD bias of 11.5 V and the results are plotted in Fig. 12. It shows that the device temperature could be set to 110 K instead of 80 K for the same photon-counting performance, consistent with the results from a similar type of HgCdTe APD arrays.[2]

3.7 Active Area

The active area of the detector was measured by scanning the light spot across a pixel in a raster pattern while recording the photon count rate with the counter. The result is shown in
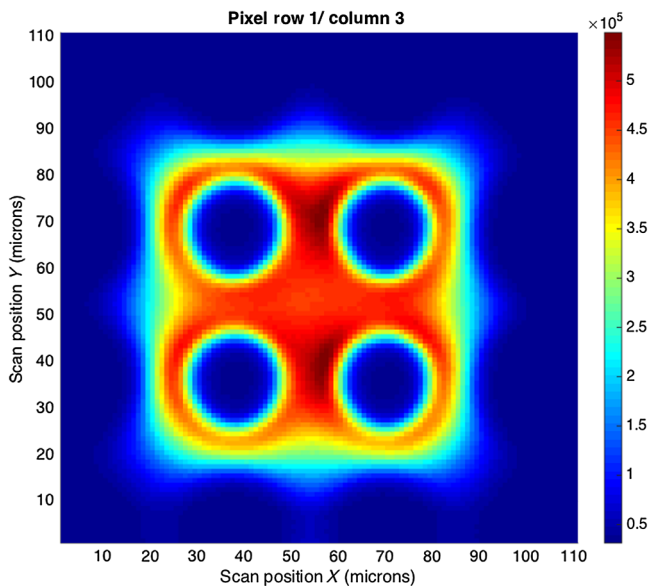

Fig. 13 Detector active area surface map obtained via a raster scan of the laser spot while measuring the photon counts of the of FPA-A8327-14-1, pixel (1,3). The APD bias voltage is set to 11.5 V.
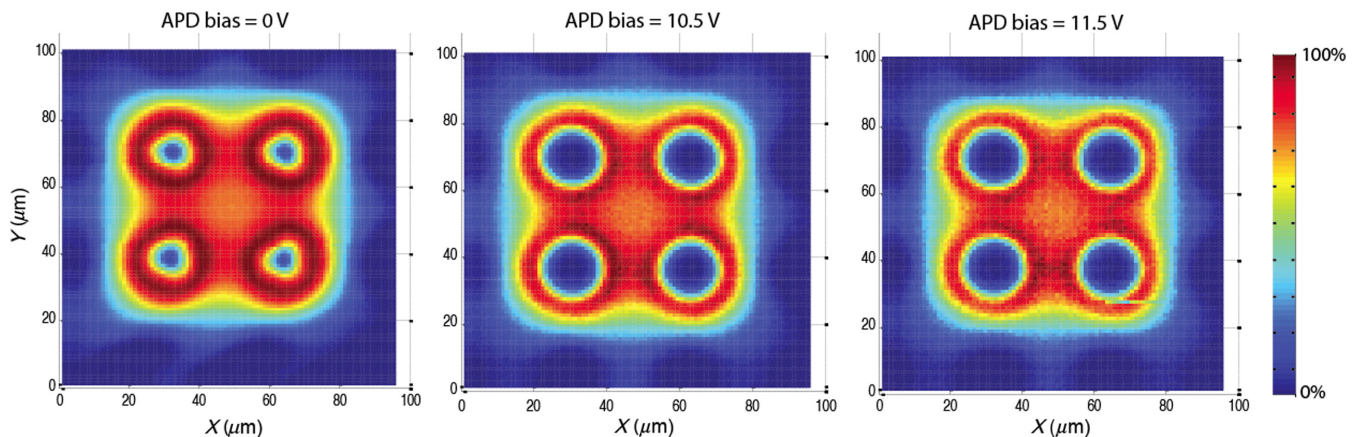
Fig. 13. There are four low signal voids, one for each of the four diodes in the pixel. The center region for optimal photon counting operation has a diameter of about 22 μm.

The detector active area in analog mode was also measured by recording the output pulse amplitude while raster scanning the laser spot at APD bias of 0, 10.5, and 11.5 V. Figure 14 shows the normalized surface map. The diameter of the signal voids increased with the APD bias due to the increasing gain in the n-region around the via, because photons falling in the via and the gain region were not multiplied by the full APD gain. These results are consistent with that predicted by the model.[18]

These results are similar to those from the earlier 4×4-pixel HgCdTe APD array with different doping profile[2] and the 2×8-pixel LMPC HgCdTe APD arrays measured at DRS.[6] They showed that the size of the void around the via changes with the p–n junctions width, which is a function of the doping and the bias voltage.

4 Test Results of the Integrated Detector Cooler Assembly

4.1 IDCA for CubeSats

As mentioned earlier, DRS developed two IDCAs under the NASA ESTO InVEST program, originally for a space demonstration on a CubeSat.[7] Two IDCAs were delivered to and tested at GSFC. Figure 15 shows a photograph of one of the delivered IDCAs. A MuMetal magnetic shield was used around the compressor specifically for the CubeSat application. An L-shaped aluminum bracket was used as the baseplate as well as the heatsink. The net mass of the cryocooler itself was 0.8 kg, including the electronics. The mass of the MuMetal magnetic shield was 350 g, and the mounting bracket was 250 g. The cooler was capable of cooling the FPA to either 80 or 110 K from an ambient temperature up to 60°C. The subsequent environmental tests were performed primarily with the detector temperature set to 110 K, because it had been shown to give the same performance as at 77 K.[2] Operating at 110 K detector temperature also significantly reduced the electrical power consumption and is expected to extend the cooler lifetime. Microlens arrays were mounted to the FPAs in both IDCA units. There were two cold filters in cascade in the Dewar with
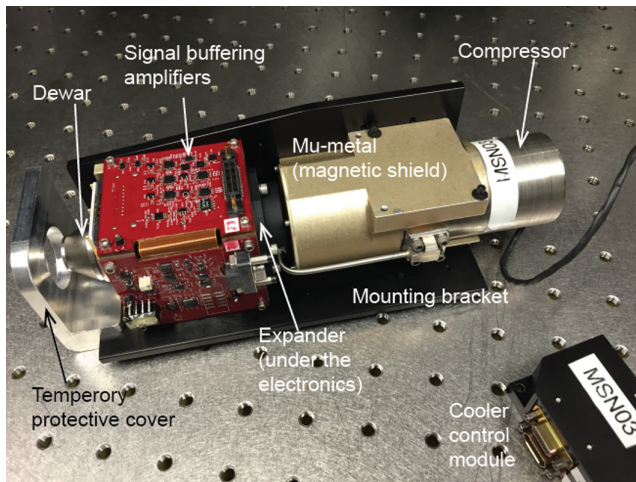

Fig. 14 Detector active area surface map of FPA-A8327-8-2, pixel (2,3), at APD bias voltage of 0, 10.5, and 11.5 V obtained by measuring the detector output pulse amplitude while scanning the laser spot position across the pixel.

Fig. 15 Photograph of the IDCA developed for a CubeSat program. It is about $7 \times 7 \times 20$ cm and fits into a 2-U CubeSat.

Fig. 16 IDCA pixel active area scan with the microlens array compared to earlier scan result without microlens array.

a passband from 0.9 to 2.1 μm. The cold shield had a numerical aperture of $f/7$, which matched the light acceptance angle of the detector with the microlens array.

A series of environmental tests were performed on the IDCAs to demonstrate their technology readiness level for the CubeSat mission.[7] These included vibration tests to verify the mechanical integrity of the unit; thermal tests to verify that the cooler and the electronics could operate over the entire temperature range predicted for the mission; and a thermal vacuum test to verify the IDCA can operate in a space-like environment. The rest of this section describes the IDCA test results.

4.2 Vibration Tests

Two vibration tests were performed at DRS. The first vibration test was performed on the cooler assembly with the detector, microlens array, and cold shield all installed but before the Dewar was capped and sealed. The subassembly was tested to 14 G rms without any damage. The second test was performed to the entire IDCA prior to delivery and it was tested to 10 G rms according to the random vibration test acceptance level of Goddard Environmental Verification Standard (GEVS) (GSFC-STD-7000) for space application.[19] The IDCA passed this test.

The vibration level of the operating cryocooler assembly was also measured. Most of the vibration came from the expander, which had a piston that moved along the cooler's long axis. The compressor used double diaphragms and most of the vibration was canceled out. When operating, the integrated vibration levels of the cryocooler assembly were found to be ~0.036 G rms along the optical (long) axis and about half that along the other two directions up to 250 Hz. The frequencies of other significant harmonics were all above 1 kHz in all three axes.

4.3 Microlens Array Performance

The microlens array stayed attached and aligned throughout the vibration and thermal tests. There was no sign of any change in the optical throughput based on the total photon count rates under the fixed illumination. A raster scan of the detector active area with the microlens array was performed
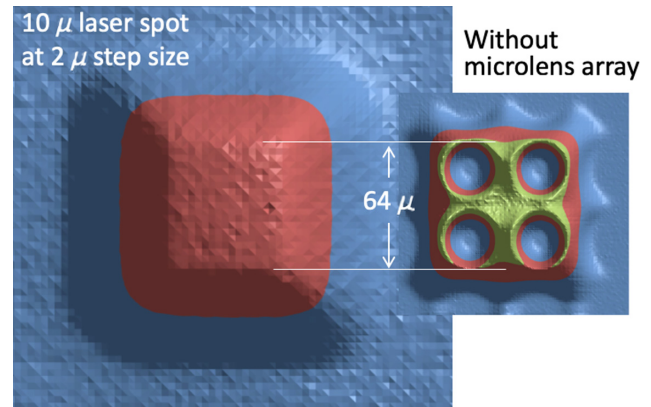
and the result is shown in Fig. 16. The light spot size in this scan was larger due to vignetting of the incident laser light by the $f/7$ cold shield and the result was not as sharp as those shown in Fig. 13. Nevertheless, it showed that the microlens array functioned as expected and improved the fill factor to nearly 100%.

4.4 Thermal Shock and Thermal Cycle Tests

A thermal shock test was performed on the IDCA at DRS by placing the IDCA in a temperature chamber at −34°C for 4 h and then moving it to another chamber at 71°C within 1 min. A thermal cycle test was also performed at DRS from −34°C to 71°C with the detector temperature set to 80 K. A hot and a cold power-on tests were performed at −24°C and 60°C ambient temperatures, respectively.

A more extended thermal test was performed at NASA GSFC from −20°C to 60°C for five more cycles, which, plus the one temperature cycle at DRS, satisfied the GSFC-STD-7000 for thermal tests. The ICDA was in a temperature chamber with circulating air and all the subsystems were thermalized to the chamber temperature. The detector temperature was set to both 80 and 110 K in this test.
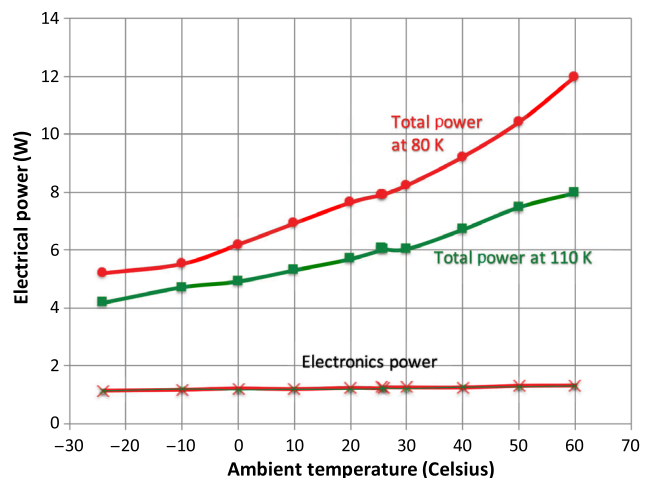

Fig. 17 Electrical power monitored the IDCA's cryocooler and the electronics (buffer amplifiers and the digital controls) during the thermal cycle test at ambient atmosphere pressure.

The detector dark count rate and the total count rate from all pixels under fixed illumination were monitored and they were consistent throughout the tests. The electrical power of the cooler and the electronics were monitored and the results are plotted in Fig. 17. The total power at room temperature was about 7 W with the detector set to 110 K and the IDCA heatsink at 40°C.

4.5 Thermal Vacuum Test

A thermal vacuum test was performed on one of the IDCA units. Four cycles were performed from −20°C to 40°C. The detector temperature was set to 110 K and regulated to ±0.1 K. The unit was covered with a thermal blanket so that the main heat path was the through heat sink (mounting bracket), of which the temperature was regulated. The temperatures of the expander and the compressor were found to be nearly the same. The electronics circuit board and the cooler control module were 5°C to 10°C warmer when the unit was powered on. The test lasted for about 2 weeks. The electrical power from the power supplies were monitored throughout the test and the results are plotted in Fig. 18. The total electrical power for the entire IDCA was between 4 and 7 W with the detector temperature at 110 K.

The detector dark count rate and total count rate were monitored throughout the tests under constant illumination. They were consistent and repeatable at a given temperature. One issue identified was the leakage of ambient thermal emission to the detector active area through the base of the cold shield and then scatter off the side to the detector as stray light. This caused the total measured "dark" count rates to vary with the Dewar body temperature by up to 100 times from the intrinsic detector dark count rate. There was also spurious leakage though the cold filter at wavelengths longer than the passband but before the detector spectral response completely cut off near 4.3 μm. A new cold filter from a different supplier has already been found that has improved out-of-band attenuation to well beyond the detector spectral response. The cold shield design has also been modified in the subsequent programs and the dark count rate has been reduced to less than those measured in the liquid nitrogen Dewar.
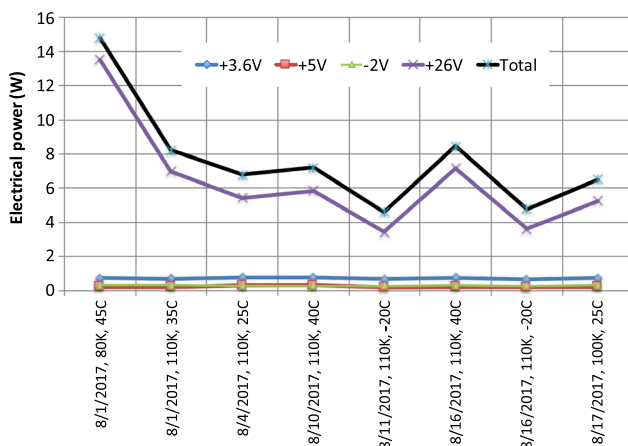

Fig. 18 Electrical power from each and all power supplies to the IDCA during the thermal vacuum test.

5 Summary

A set of LMPC HgCdTe APD FPA's were developed. One of them was packaged into an environmentally rugged IDCA. The APD arrays had 2×8 pixels with 64×64-μm pixel size and 64-μm spacing. The test results showed that the photon detection efficiency was as high as 70% at a dark count rate of 250 kHz and the timing jitter was <0.5 ns. The devices produced a linear analog waveform output from each pixel with several orders of magnitude of dynamic range. The IDCA was developed using a ruggedized mini-Stirling cryocooler for airborne and spaceborne lidar. A microlens array was integrated with the APD array and was shown to improve the detector's fill factor to nearly 100%. The IDCA assembly passed vibration, thermal cycle, and thermal vacuum tests at the NASA GEVS levels. A series of radiation tests were also performed which showed that the devices can be used in multiyear Earth orbiting or planetary space mission.

Acknowledgments

References

1. J. D. Beck et al., "Linear mode photon counting with the noiseless gain HgCdTe e-avalanche photodiode," *Opt. Eng.* **53**(8), 081905 (2014).
2. X. Sun et al., "HgCdTe avalanche photodiode detectors for airborne and spaceborne lidar at infrared wavelengths," *Opt. Express* **25**(14), 16589–16602 (2017).
3. J. Abshire et al., "Airborne measurements of CO_2 column concentrations made with a pulsed IPDA lidar using multiple-wavelength-locked laser and HgCdTe APD detector," *Atmos. Meas. Tech.* **11**, 2001–2025 (2018).
4. H. Riris et al., "Methane optical density measurements with an integrated path differential absorption lidar from an airborne platform," *J. Appl. Remote Sens.* **11**(3), 034001 (2017).
5. T. Refaat et al., "MCT avalanche photodiode detector for two-micron active remote sensing applications," in *IEEE Int. Geosci. Remote Sens. Symp. (IGARSS)*, Paper TU2.R9.4 (2018).
6. W. Sullivan, III et al., "Linear-mode HgCdTe avalanche photodiodes for photon-counting applications," *J. Electron. Mater.* **44**(9), 3092–3101 (2015).
7. R. Fields et al., "A linear mode photon-counting (LMPC) detector array in a CubeSat to enable earth science LIDAR measurements," in *IEEE Int. Geosci. and Remote Sens. Symp. (IGARSS)*, Paper FR2.B1 (2015).
8. X. Sun et al., "Single photon HgCdTe avalanche photodiode and integrated detector cooler assemblies for space lidar applications," *Proc. SPIE* **10659**, 106590C (2018).
9. X. Sun et al., "Evaluation of space radiation effects on HgCdTe avalanche photodiode arrays for lidar applications," *Proc. SPIE* **10624**, 1062415 (2018).
10. J. Beck et al., "The HgCdTe electron avalanche photodiode," *J. Electron. Mater.* **35**(6), 1166–1173 (2006).
11. M. A. Kinch, *Fundamental of Infrared Detector Materials*, pp. 493–512, SPIE Press, Bellingham, Washington (2007).
12. I. Baker and M. Kinch, "HgCdTe electron avalanche photodiodes (EAPDs)," Chapter 21 in *Mercury Cadmium Telluride: Growth, Properties and Applications*, P. Capper and J. Garland, Ed., John Wiley & Sons, Chichester (2011).
13. M. A. Kinch, *State-of-the-Art Infrared Detector Technology*, SPIE Press, Bellingham, Washington (2014).
14. A. Veprik et al., "Compact linear split Stirling cryogenic cooler for high temperature infrared imagers," in *Proc. 16th Int. Cryocooler Conf.*, Atlanta, Georgia, pp. 17–20 (2010).
15. D. Rawlings and G. Averitt, "A linear drive cryocooler for ultra-small infrared sensor systems," *Proc. SPIE* **9070**, 90702R (2014).
16. J. Raab and E. Tward, "Northrop Grumman aerospace systems cryocooler overview," *Cryogenics* **50**, 572–581 (2010).
17. H. W. Southwell, "Focal-plane pixel-energy redistribution and concentration by use of microlens arrays," *Appl. Opt.* **33**(16), 3460–3464 (1994).

18. J. Beck, M. Kinch, and X. Sun, "Update on linear mode photon counting with the HgCdTe e-APD," *Opt. Eng.* **53**(8), 081906 (2014).
19. Goddard Environmental Verification Standard, GSFC-STD-700, https://standards.nasa.gov/standard/gsfc/gsfc-std-7000 (accessed 25 January 2019).

Xiaoli Sun is a research physical scientist at the Planetary Geology, Geophysics, and Geochemistry Laboratory, NASA Goddard Space Flight Center (GSFC). He received his BS degree from Taiyuan Institute of Technology, Taiyuan, China, in 1982, and his MS degree and PhD in electrical engineering from Johns Hopkins University, Baltimore, Maryland, in 1985 and 1989, respectively. He was an instrument scientist for the Mercury Laser Altimeter on the MESSENGER mission, the Lunar Orbiter Laser Altimeter, and the one-way Laser Ranging system on the Lunar Reconnaissance Orbiter (LRO) mission. He has recently been leading the research and applications of HgCdTe avalanche photodiode (APD) arrays at GSFC for future NASA swath mapping lidar and spectroscopic infrared lidar in space.

James B. Abshire is the senior scientist for laser remote sensing for the solar system exploration division at NASA's GSFC. He has helped lead the development of space lidar at Goddard and was instrument scientist on the Mars Orbiter Laser Altimeter on the Mars Global Surveyor Mission and the Geoscience Laser Altimeter System on the ICESat Mission. Currently, he is leading Goddard's work in remotely measuring atmospheric CO_2 with lidar and serves on the formulation teams for the NASA ASCENDS mission and the French/German MERLIN mission. He received his PhD in electrical engineering from the University of Maryland in 1982, and his BS degree in electrical engineering from the University of Tennessee in 1974.

Michael A. Krainak received his BS degree in electrical engineering from Catholic University and his MS degree and PhD in electrical engineering from Johns Hopkins University. He started his career as a telephone switch office field engineer for AT&T Western Electric. He worked for 10 years at the National Security Agency in signal processing, Fourier optics, and microelectronic circuit design. For the past 22 years, he has worked at NASA GFSC on intersatellite laser communications and lidar. Currently, he is the head of the Laser and Electro-Optics Branch at NASA GSFC.

Wei Lu received his BS degree from Shanghai University of Technologies, China, in 1989, and his MS degree from Shanghai Institute of Technical Physics, Chinese Academy of Sciences, in 1996, both in electrical engineering. Currently, he is a senior staff engineer of ATA Aerospace, LLC at NASA's GSFC, Greenbelt, Maryland. He is the lead engineer in hyperspectral FPA detector of Ocean Color Instrument (OCI) on the PACE mission. His primary focus is detector technologies, optical communication and ranging, and electronic circuit design.

Jeff D. Beck received his MSEE and BSEE degrees from MIT, Cambridge, Massachusetts, in 1972. He joined Texas Instruments in 1978 and was elected Distinguished Member Technical Staff in 1996. He received his Military Sensing Symposium (MSS) Herschel Award on behalf of DRS in 2004 for the noiseless gain HgCdTe APD. He was elected MSS fellow in 2006. He won the international "Innovation Award 2009" from Finmeccanica S.p.A, Rome, Italy. He is a staff scientist at Leonardo DRS, Dallas, Texas.

William W. Sullivan, III received his BS and MS degrees and his PhD in electrical engineering from Texas Tech University in Lubbock, Texas, in 2008, 2009, and 2013, respectively. Currently, he is researching APDs for photon-counting applications at DRS Technologies in Dallas, Texas. His research interests include device physics, APDs, infrared imaging systems, and compact pulsed power technology.

Pradip Mitra received his MSc degree from the Indian Institute of Technology, Kanpur, India, and his PhD from Boston University, Boston, Massachusetts. In his 25-year career, he has been involved in IR materials and detector research. After working at Lockheed Martin for 13 years, he joined DRS Technologies in Dallas, Texas. At DRS, he is currently the senior director of advanced development programs where he oversees multiple IR technology development activities that include active imaging detectors and sensors.

Dick M. Rawlings received his BMechE from the University of Minnesota in 1978 and an MSME from Southern Methodist University in 1985. He has been involved in developing cryogenic coolers and Dewars for infrared sensor applications at Leonardo DRS in Dallas, Texas, for over 40 years. He holds a patent for cryogenic cooler design. Currently, he is developing integrated Dewar cooler assemblies (IDCAs) for advanced IR FPAs.

Renny A. Fields has been involved in laser source development and laser sensor systems engineering for his entire 34 year career at The Aerospace Corporation. He is a corporate technical fellow in the Electronics and Photonics Laboratory and is currently the PI on the MAFIOT Mt. Wilson Ground station, the ARX strategic GEO crosslink, and the NASA LMPC Cubesat. He was the PI on the NFIRE laser communication experiment in collaboration with the German MOD, the DLR and Tesat, as well as a key advisor to the government on several space LADAR sensors both planned and in orbit. He also served as general chair of the CLEO conference in 2002. He has a PhD in chemical physics from the University of Chicago.

David A. Hinkley has been a member of the PICOSAT program, the Aerospace Corporation's miniature satellite effort since its inception in 1998 to present. He has performed the diverse roles of designer, builder, and project manager for four miniature satellite missions that rode into space and were ejected from the space shuttle in 2002, 2006, 2008, and 2011 and for the AeroCube flown in 2006, 2007, and 2009. More recently, he was principal engineer for AeroCube missions in 2012, 2016 and 2019. He has a BS degree in mechanical engineering from UCSD and an MS degree in manufacturing engineering with emphasis in robotics from UCLA and holds five patents.

Bradley S. Hirasuna is an assistant general manager in the Office of the Chief Technology Officer at The Aerospace Corporation. He is responsible for supporting the vice president and CTO as the deputy for technology integration. In addition, he leads the Strategy Integration Office, which integrates activities in the innovation office, iLab, science and technology hubs, and prototyping group, xLab.